

PHYSICS

An experimental test of the geodesic rule proposition for the noncyclic geometric phase

Zhifan Zhou¹, Yair Margalit^{1,2}, Samuel Moukouri¹, Yigal Meir^{1*}, Ron Folman¹

The geometric phase due to the evolution of the Hamiltonian is a central concept in quantum physics and may become advantageous for quantum technology. In noncyclic evolutions, a proposition relates the geometric phase to the area bounded by the phase-space trajectory and the shortest geodesic connecting its end points. The experimental demonstration of this geodesic rule proposition in different systems is of great interest, especially due to the potential use in quantum technology. Here, we report a previously unshown experimental confirmation of the geodesic rule for a noncyclic geometric phase by means of a spatial SU(2) matter-wave interferometer, demonstrating, with high precision, the predicted phase sign change and π jumps. We show the connection between our results and the Pancharatnam phase. Last, we point out that the geodesic rule may be applied to obtain the red shift in general relativity, enabling a new quantum tool to measure gravity.

INTRODUCTION

The geometric phase (GP), the phase acquired over the course of an evolution of the Hamiltonian in parameter space, is a central concept in classical and quantum physics (1–9). Originally, the GP was defined only for an evolution of a system in a closed trajectory in phase space, but later, it was generalized to noncyclic evolutions (7, 10). For the case of a two-level system, where the evolution of the system can be described by a trajectory on the Bloch or Poincaré spheres, it has been proposed (7, 10) that, using a natural definition of the phase (1), the GP is given by half the area enclosed by the trajectory and the geodesic connecting the initial and final points. A marked outcome of the proposed geodesic rule is that this noncyclic phase changes sign when the trajectory moves from the upper to the lower hemisphere, resulting in a π -phase jump when the trajectory is half the circumference of a circle (7, 10). While the GP for a closed trajectory has been measured experimentally in several physical systems in a fairly straightforward manner (11–15), the experimental verification of the GP during noncyclic evolution requires a more convoluted approach. This is so because the cyclic GP can be readily measured as the probed state is returned to its initial position in parameter space, where it can be compared with a reference state to measure the relative phase, while for noncyclic geometric evolutions, where the probed state is not returned to its initial position, one needs to project the final state onto the initial state. Using an ultracold atom spatial interferometer, we test the geodesic rule, including the predicted SU(2) phase sign change and π jumps.

Berry's original work (2) addressed a quantum system undergoing a cyclic evolution under the action of a time-dependent Hamiltonian. When the Hamiltonian returns to its initial value, the quantum state acquires an extra GP in addition to the dynamical phase. This concept has been generalized (7) to a noncyclic evolution of the system, where the parameters of the Hamiltonian do not return to their initial values. In addition to the fundamental interest in better understanding the noncyclic behavior, it may also prove to be technolog-

ically advantageous. For example, as the system does not need to return to its original state, geometric operations may be done faster, e.g., geometric quantum gates (16–18). Quantum optimal control of the evolution may also benefit (19, 20). In addition, metrology may be made more sensitive due to the expected phase sign change and phase jumps, e.g., in measuring a gravitational potential (21).

The geometric interpretation of this noncyclic GP takes an illuminative form for a two-level system whose state can be described by two angles, $\Psi = (\cos \frac{\theta}{2} | 2\rangle + \exp(i\phi) \sin \frac{\theta}{2} | 1\rangle)$, which define a point on the Poincaré or Bloch spheres. The propagation of a state under a noncyclic evolution of the Hamiltonian, from Ψ_A to Ψ_B , characterized by $\{\theta_A, \phi_A\}$ and $\{\theta_B, \phi_B\}$, respectively, is represented by a curve connecting points A and B on the sphere. Using a natural definition of the phase (1), where the relative phase between two arbitrary states is zero when the visibility of their interference pattern is maximal, the GP associated with this propagation is determined by the geodesic rule: it is given by half the area on the sphere bordered by the evolution curve and the shortest geodesic connecting A and B (22). An illustration of the geodesic rule on the Bloch sphere is shown in Fig. 1, where A evolves toward B , along the latitude of fixed $\theta_A = \theta_B = \theta$, and ϕ changes from ϕ_A to $\phi_B = \phi_A + \Delta\phi$ (the curve C_{AB}). The area corresponding to the GP, blue shaded in the figure, is enclosed by C_{AB} and by the geodesic curve G_{AB} joining points A and B . If C_{AB} is on the northern hemisphere, G_{AB} is above (toward the north pole) C_{AB} . But if C_{AB} is on the southern hemisphere, G_{AB} is below C_{AB} , leading to a sign change of the GP as C_{AB} crosses the equator.

Since the introduction of the geodesic rule, several studies have verified it experimentally with light (23, 24), neutron (25, 26), and atom (27, 28) interferometers [see also (29) and (30) for relevant debates and (31) for other interpretations]. In this work, we propose and realize a matter-wave experimental study using cold-atom spatial interferometry (32, 33). The uniqueness of our approach includes (i) the use of a spatial interference pattern to determine the phase in a single experimental run (no need to scan any parameter to obtain the phase), (ii) the use of a common phase reference for both hemispheres and a scan of θ enabling to verify the π phase jump and the sign change, and (iii) obtaining the relative phase by allowing Ψ_A and Ψ_B to expand in free flight and overlap, different from previous atom-interferometry studies that required, for obtaining interference, an

¹Department of Physics, Ben-Gurion University of the Negev, Beer-Sheva 84105, Israel. ²Research Laboratory of Electronics, MIT-Harvard Center for Ultracold Atoms, Department of Physics, Massachusetts Institute of Technology, Cambridge, MA 02139, USA.

*Corresponding author. Email: ymeir@bgu.ac.il

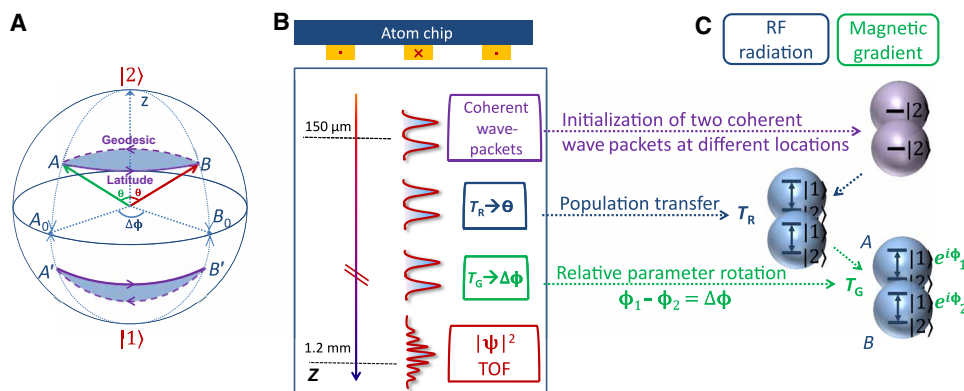


Fig. 1. Illustration of the geodesic rule and the experimental sequence. (A) An illustration of the geodesic rule (7, 10) on the Bloch sphere representing the two-dimensional space defined by our physical two-level system. The green and red arrows represent the internal states A and B of the two spatially separated wave packets, Ψ_A and Ψ_B (see Eq. 1). The rotation angle from the north pole θ and the rotation $\Delta\phi$ along the latitude (continuous purple) represent the $SU(2)$ operations applied in the experiment, where the former requires an RF pulse, while the latter requires a magnetic gradient. When $\theta = \pi/2$, the arrows lie on the equator of the Bloch sphere (A_0 and B_0). The dashed purple curve is the geodesic joining points A (A') and B (B'). The GP is equal to one-half of the blue area enclosed by the latitude and geodesic. The area's orientation (indicated by the arrows) is determined by the geodesic rule. It is negative, counterclockwise (northern hemisphere) and positive, clockwise (southern hemisphere). (B) Experimental sequence (not to scale) of the longitudinal interferometer. The experiment is performed in free fall. The final interference pattern (from which the total phase is obtained) develops after time-of-flight (TOF) free evolution, in which the two wave packets expand and overlap. The pattern is then recorded by a CCD camera. (C) Evolution of the states during the sequence. After the preparation of two coherent wave packets at different locations, an RF pulse of duration T_R is applied to manipulate θ , and a magnetic field gradient of duration T_G is applied to manipulate $\Delta\phi$.

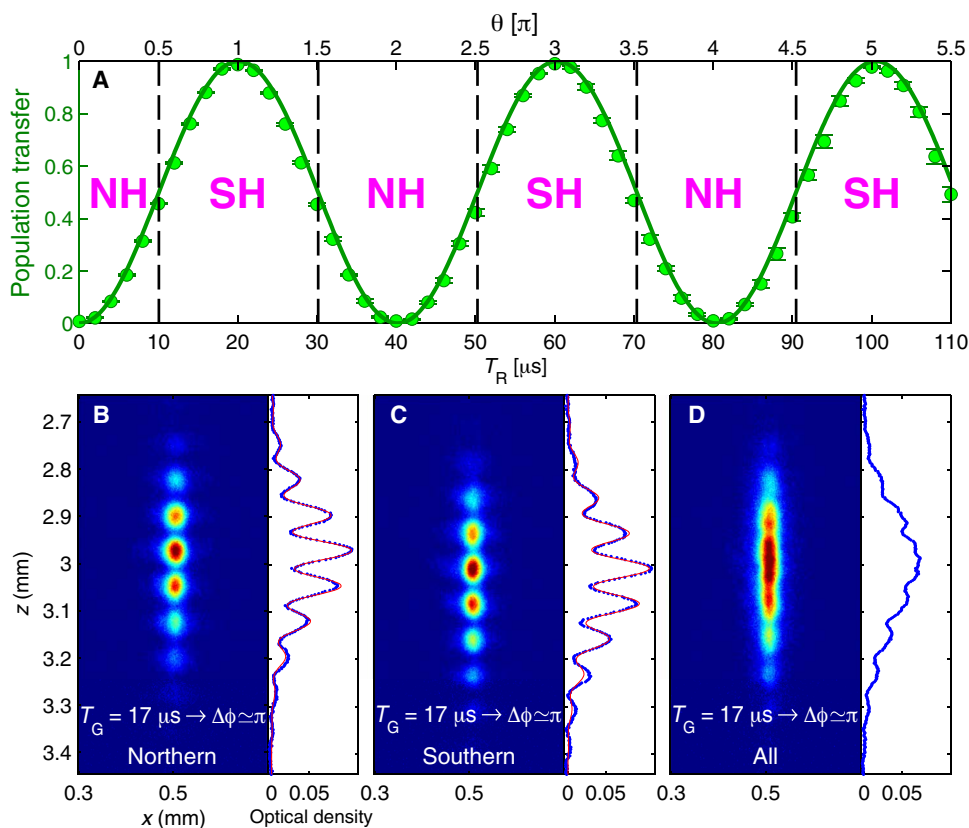


Fig. 2. Population transfer and its connection to the π phase jump. (A) Population transfer to state $|1\rangle$ versus the duration of the RF radiation pulse T_R , for which $20 \mu\text{s}$ corresponds to total population transfer ($\theta = \pi$ in Fig. 1). With this independent measurement, we determine θ for our $SU(2)$ operations. (B) Averaged CCD image of interference when the Bloch vectors are all in the northern hemisphere [NH data points specified in (A)], with $\Delta\phi \approx \pi$. The high visibility indicates the existence of phase rigidity, namely, that the phase is independent of θ . The phase returned by the fit is 1.13 ± 0.02 rad relative to a fixed reference point, and the visibility is 0.55 ± 0.01 (see Methods for the definition). (C) Averaged picture of the second half of the data, in which the Bloch vectors are all pointing in the southern hemisphere [SH data points specified in (A)], with $\Delta\phi \approx \pi$. A phase jump is clearly visible. The phase is 4.34 ± 0.03 rad relative to the fixed reference point, which is common to both pictures, and the visibility is 0.52 ± 0.01 . The phase difference between (B) and (C) is thus 3.21 ± 0.05 rad, close to π . The data included in these images (in total, about 330 consecutive experimental shots without post-selection or post-correction) are presented in Fig. 3B. (D) Averaged picture of all the data for $\Delta\phi \approx \pi$. The visibility is 0.03 ± 0.01 . The low visibility shows that the phase jump has a value close to π . Single-shot data are presented in Fig. 3B, and single-shot images are presented in Fig. 6.

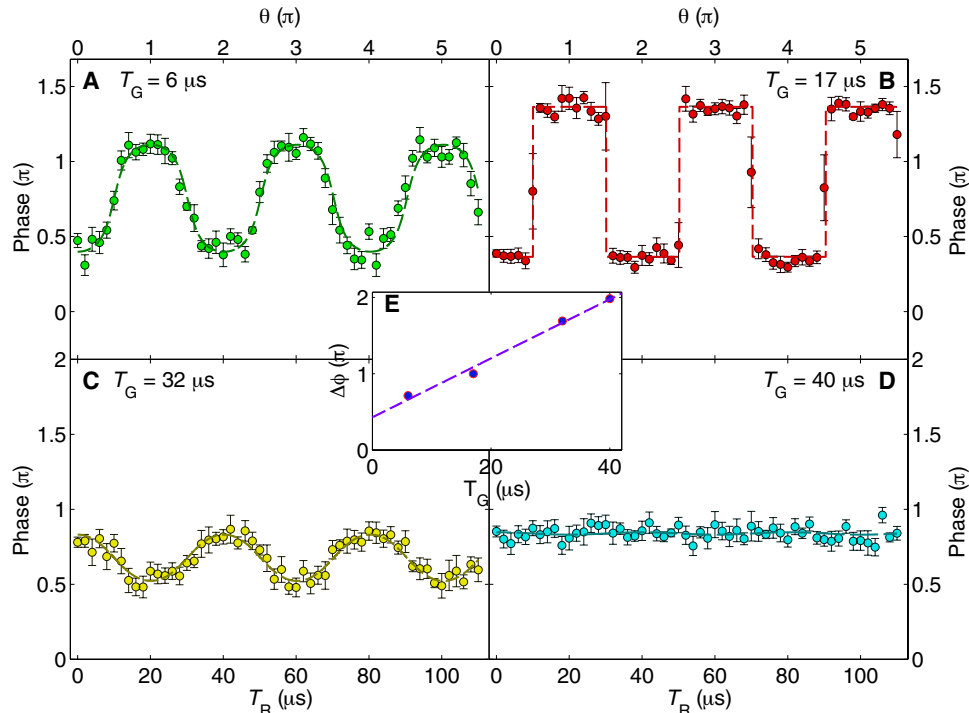


Fig. 3. The phase of the interference pattern: Phase jump and rigidity. (A to D) Total phase Φ as a function of T_R (θ) for T_G is equal to 6, 17, 32, and 40 μs . Each data point is an average of six experimental cycles (errors are SEM). The dashed lines are a fit to Eq. 2, which allows us to determine $\Delta\phi$ for our SU(2) operations. The fit returns the values $\Delta\phi = 2.24$ (A), $\Delta\phi = 3.14$ (B), $\Delta\phi = 5.31 \equiv 2\pi - 0.97$ (C), and $\Delta\phi = 6.23 \equiv 2\pi - 0.05$ (D) radians, respectively (manifested in the graph as the peak-to-valley amplitude if we consider the periodicity of 2π when defining a phase). The fit also returns a baseline phase ϕ_0 . Last, the phase rigidity and the phase jump observed in Fig. 2 are clearly visible in (B). (E) Linear mapping from T_G to $\Delta\phi$. As seen in the graph ($T_G = 0$), we have a fixed background gradient equivalent to $\Delta\phi = 1.35$.

additional manipulation of the SU(2) parameters θ and $\Delta\phi$. As a result of our novel technique, we are able to test and confirm the geodesic rule for noncyclic evolutions in a new way, including the predicted sign change and the predicted SU(2) phase jumps.

EXPERIMENT

Our full experimental procedure is detailed elsewhere (34–36) as well as in Methods and the Supplementary Materials. The relevant part for the determination of the GP is sketched in Fig. 1. The ^{87}Rb atom can be in either state $|1\rangle \equiv |F=2, m_F=1\rangle$ or $|2\rangle \equiv |F=2, m_F=2\rangle$, where F is the total angular momentum and m_F is the projection. We start by preparing two-atom wave packets at different positions, both in an internal state $|2\rangle$. We first apply a uniform radio-frequency (RF) pulse, of time duration T_R , which transfers population from the $|2\rangle$ state to $|1\rangle$, shifting both wave packets from the north pole of the Bloch sphere to a point whose latitude θ depends on T_R (Fig. 1A). We then apply a magnetic field gradient pulse of duration T_G , which results, due to the different magnetic moments of states $|1\rangle$ and $|2\rangle$, in a phase difference between these states, rotating both superpositions along a constant latitude on the Bloch sphere. Because of the difference in positions, each wave packet experiences a different magnetic field and thus will rotate by a different angle, ending up at points A and B in Fig. 1A. The two states, after the application of both T_R and T_G , can thus be written as

$$\begin{aligned} \Psi_A &= \psi_A(r) \left(\cos \frac{\theta}{2} |2\rangle + \sin \frac{\theta}{2} |1\rangle \right) \\ \Psi_B &= \psi_B(r) \left(\cos \frac{\theta}{2} |2\rangle + \exp(i\Delta\phi) \sin \frac{\theta}{2} |1\rangle \right) \end{aligned} \quad (1)$$

where θ is proportional to T_R , and $\Delta\phi$ to T_G . $\psi_A(r)$ and $\psi_B(r)$ are the spatial components of the respective states. There may also be an additional global phase, identical for both Ψ_A and Ψ_B , which plays no role in the interference between Ψ_A and Ψ_B . To measure this interference, we allow enough time of flight for the two wave packets to free fall, expand, and overlap, before taking a picture using a charge-coupled device (CCD) camera.

RESULTS

Figure 2 depicts the averaged interference patterns (raw data CCD images) averaged over all values of θ in the upper (B) or lower (C) hemispheres, for $T_G = 17 \mu\text{s}$ ($\Delta\phi \approx \pi$). The value of θ was independently deduced from the relative populations of states $|1\rangle$ and $|2\rangle$, which are given by $\cos^2(\theta/2)$ and $\sin^2(\theta/2)$, respectively (Figs. 2A and 5). The high visibility in both images indicates the existence of “phase rigidity,” namely, that the measured phase is independent of θ in each hemisphere. Moreover, the two datasets have a phase difference of π , which can also be deduced from the vanishing visibility in Fig. 2D, where the two datasets in (B) and (C) are joined. Evidently, there is a sharp jump in the phase of the interference pattern as θ crosses the equator.

According to Eq. 1, the interference phase Φ , for general θ and $\Delta\phi$, is given by

$$\Phi = \arg \langle \Psi_A | \Psi_B \rangle = \phi_0 + \arctan \left\{ \frac{\sin^2(\theta/2) \sin \Delta\phi}{\cos^2(\theta/2) + \sin^2(\theta/2) \cos \Delta\phi} \right\} \quad (2)$$

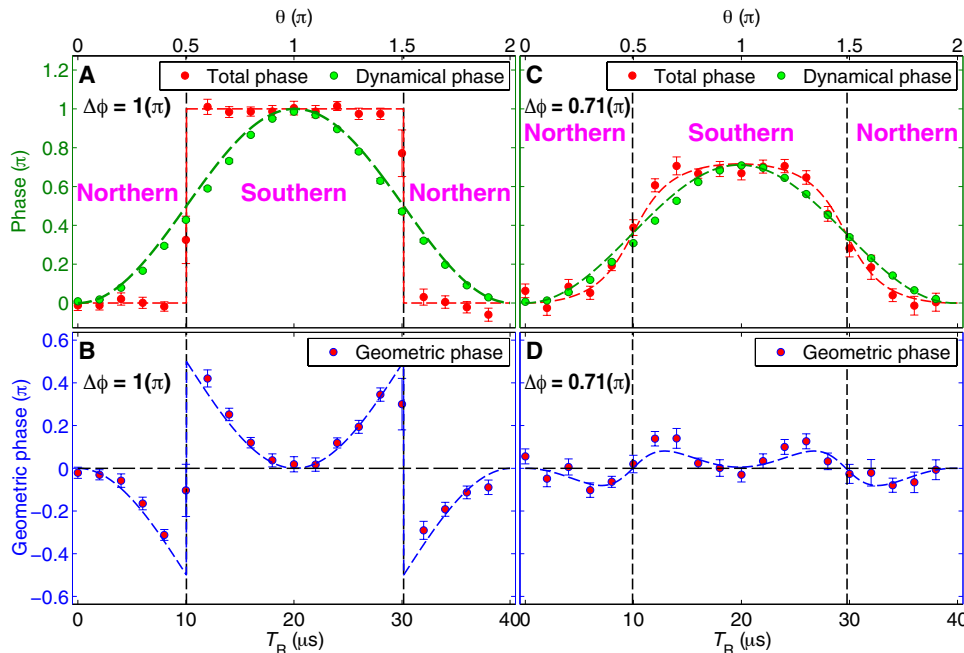


Fig. 4. Geometric SU(2) phase jump and sign flip, experiment (dots) versus theory (Eq. 3, dashed lines). (A) Total phase and dynamical phase for $\Delta\phi = \pi$ as a function of T_R (θ). The total phase is directly measured from the imaged interference pattern (Fig. 3), and the dynamical phase $\frac{\Delta\phi}{2}(1 - \cos \theta)$ is deduced from the independently measured values of θ and $\Delta\phi$. (B) GP Φ_G determined as the difference between the two sets of points appearing in (A). The predicted sign change as the latitude crosses the equator is clearly visible. The evident phase jump is due to the geodesic rule. When $\Delta\phi = \pi$, the geodesic must go through the Bloch sphere pole for any $\theta \neq \pi/2$. As the latitude approaches the equator (i.e., increasing θ), the blue area in Fig. 1 (twice Φ_G) continuously grows to reach a maximum of π in the limit of $\theta = \pi/2$. As the latitude crosses the equator, the geodesic jumps from one pole to the other pole, resulting in an instantaneous change of sign of this large area and a phase jump of π . This plot exactly confirms the prediction in (10). (C) Total phase and dynamical phase for $\Delta\phi = 2.24$ rad (0.71π). (D) Φ_G , determined as the difference between the two sets of points appearing in (C). The predicted sign change is again visible. However, in the case of $\Delta\phi = 2.24$ rad (0.71π), the geodesic line does not go through the pole, and as the latitude approaches the equator, Φ_G actually reduces (after reaching its maximum for an intermediate θ), so no abrupt phase jump is expected.

where $\phi_0 = \arg \langle \psi_A(r) | \psi_B(r) \rangle$ is the phase associated with the evolution of the external degrees of freedom of the system (see Methods). Figure 3 depicts the interference phase, deduced from the raw data, as a function of T_R for different values of T_G . The dashed lines in this figure are a fit to Eq. 2, with the fitting parameters ϕ_0 (an overall vertical shift) and $\Delta\phi$. The excellent fit to the data allows us to determine with high precision the values of $\Delta\phi$ (Fig. 3E).

The total phase (interference phase) Φ is a sum of two contributions, the GP Φ_G and the dynamical phase Φ_D . While both Φ and Φ_D are gauge dependent, $\Phi_G = \Phi - \Phi_D$ is gauge independent (37, 38). Substituting for the dynamical phase (6, 10, 37, 38), we obtain (see Methods)

$$\Phi_G = \arctan \left\{ \frac{\sin^2(\theta/2) \sin \Delta\phi}{\cos^2(\theta/2) + \sin^2(\theta/2) \cos \Delta\phi} \right\} - \frac{\Delta\phi}{2}(1 - \cos \theta) \quad (3)$$

where the gauge-dependent phase ϕ_0 has dropped out.

Figure 4 displays Φ , Φ_D , and the resulting Φ_G , for two values of $\Delta\phi$, where the first term on the right-hand-side of Eq. 3 is given by Φ , the phase of the interference pattern, while the second is evaluated for the experimentally determined values of θ and $\Delta\phi$. The dashed lines in Fig. 4 (B and D) correspond to the geodesic rule—half the area between the geodesic and the trajectory, with the correct sign. A very good agreement between data and the theoretical predictions is observed. This constitutes a complete verification of the GP asso-

ciated with noncyclic evolution in an SU(2) system and accurately confirms the theoretical predictions, including a precise observation of the geodesic rule, the phase sign change, and the π phase jump.

DISCUSSION

Last, we make a fundamental connection between our experiment and the Pancharatnam phase (1). We begin by noting that in the case $\phi_0 = 0$, we have $\arg \langle \Psi_A | 2 \rangle = 0$ and $\arg \langle 2 | \Psi_B \rangle = 0$, and then the states A , $|2\rangle$, and B fulfill the Pancharatnam consecutive in-phase criterion (1, 22). It then follows that $\arg \langle A | B \rangle$ is given by half the area σ of the spherical triangle defined by these three states on the Bloch sphere, namely, the area in between three geodesic lines. The area σ of the spherical triangle defined by the two arcs joining the north pole and points A and B is given by the relation $\tan(\sigma/2) = \tan_2(\theta/2) \sin(\phi) / [1 + \tan_2(\theta/2) \cos \phi]$, which is identical to Eq. 2 with $\Phi = \sigma/2$ (for $\phi_0 = 0$). This geometric interpretation of Φ yields an explanation of the observed phase rigidity for $\Delta\phi = \pi$: When the two points are in the northern hemisphere, the geodesic between the two points goes through the north pole. The enclosed area is zero; hence, $\Phi = 0$. When the two points are in the southern hemisphere, the geodesic goes through the south pole, with an area of 2π , resulting in a jump of π in the value of Φ (Fig. 2). The geometric interpretation of our experiment is now evident, namely, what is measured in the experiment (the interference-pattern phase) is the Pancharatnam phase Φ_P . The difference between the areas associated with Φ_P and Φ_D gives the light blue area in Fig. 1, associated

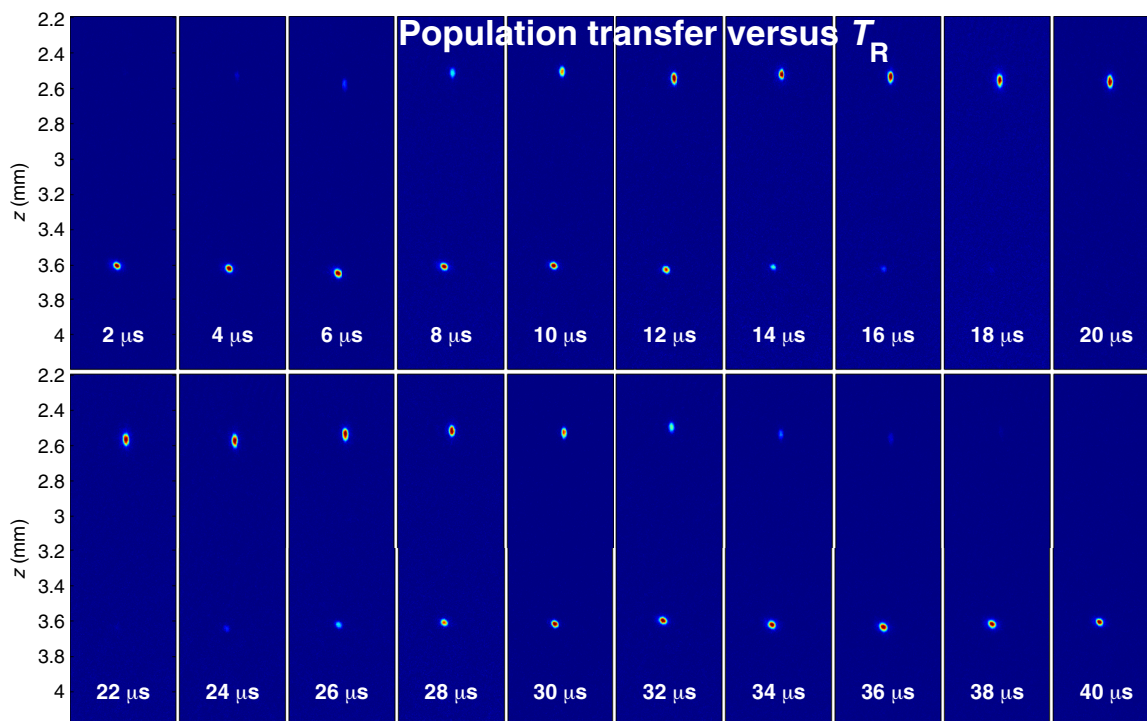


Fig. 5. The population transfer versus T_R is measured in an independent experiment by applying a strong magnetic gradient after T_R . Because of the Stern-Gerlach effect, the $m_f = 1$ and $m_f = 2$ parts are shifted to different regions of space when the absorption imaging is performed to evaluate the atom number. The absorption imaging is based on the comparison between the intensity I of a light pulse going through the atoms and the intensity I_0 of a reference light pulse that propagates in the absence of atoms and the Beer's law, $I(x_i, z_j) = I_0(x_i, z_j)e^{-OD(x_i, z_j)}$. The optical density (OD) is proportional to the column density of the atoms at a given position $\int n(x, y, z)dy$, where x and z are the object plane positions corresponding to x_i and z_j , respectively. The number of atoms $N(x_i, z_j)$ imaged by the pixel is $N(x_i, z_j) = \frac{A}{\sigma_0} OD(x_i, z_j)$, where A is the pixel area in the object plane, $\sigma_0 = 3\lambda^2/2\pi$ is the cross section for resonant atom-light scattering, and $\lambda \approx 780$ nm is the optical transition wavelength. The total atom number is equal to $\int N(x, z)dx dz$. We can then reliably determine the relation between population transfer and T_R as presented in Fig. 2A, e.g., $10 \mu\text{s}$ corresponds to $\theta = \pi/2$, $20 \mu\text{s}$ corresponds to $\theta = \pi$, and $40 \mu\text{s}$ corresponds to $\theta = 2\pi$.

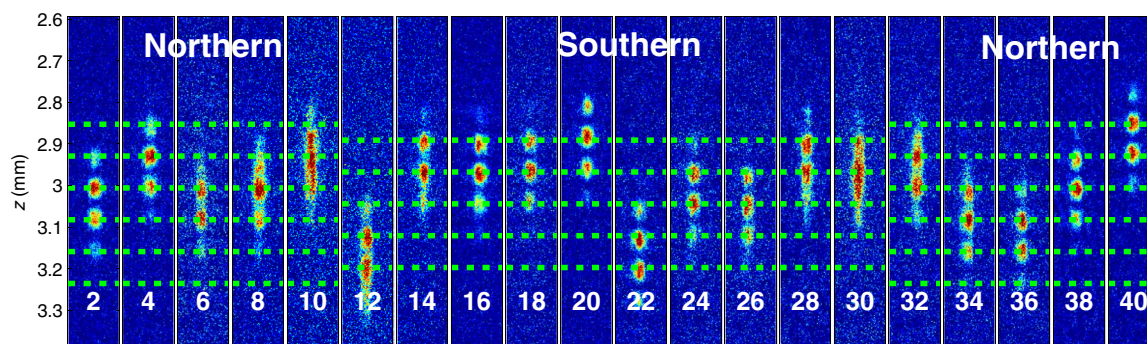


Fig. 6. The interference pattern versus T_R when $T_G = 17 \mu\text{s}$ ($\Delta\phi \approx \pi$). The number in each subfigure indicates the duration of T_R in microseconds. When the Bloch vectors are in the northern hemisphere, the interference phase is seen to be rigid (fixed). When the Bloch vectors cross the equator at $T_R = 10 \mu\text{s}$, there is a π phase jump. The interference phase will jump by another π when the vectors cross the equator again at $T_R = 30 \mu\text{s}$. Namely, phase rigidity appears when the Bloch vectors are located in either the northern or southern hemisphere, with a π phase jump in between, as presented in Fig. 2 (B to D) and Fig. 3B. The fluctuations in the interference pattern's location are due to fluctuations in the initial conditions from shot to shot, while the inferred phase is stable, as explained in (34).

with Φ_G . This now naturally explains both the sign change of Φ_G as the latitude crosses the equator, as well as the phase jump for $\Delta\phi = \pi$ (Fig. 4).

OUTLOOK

As an outlook, we consider a situation in which the two wave packets are viewed as a split wave packet of a single clock, where $\theta = \pi/2$

for a perfect two-level clock (35, 36). When we place the two wave packets along a vertical line parallel to gravity at different distances from earth, they are exposed to different proper times. In the experiment described in this paper, the relative phase $\Delta\phi = \Delta(E_1 - E_2) \times t/\hbar$ between the wave packets is determined by a magnetic gradient, which changes the energy splitting $E_1 - E_2$ between states $|1\rangle$ and $|2\rangle$ [i.e., $\Delta(E_1 - E_2)$ is the difference of energy splitting between two

wave packets Ψ_A and Ψ_B], while time (from the moment the two wave packets were allowed to free fall) is the same for both wave packets. However, the same GP situation occurs when the magnetic gradient is zero and consequently the splitting $E_1 - E_2$ is identical for the two wave packets, but time elapsed is different for the two wave packets due to the different red shift (with time difference Δt). In this case, we have $\Delta\phi = (E_1 - E_2) \times \Delta t/\hbar$, and the same theory presented in this paper may be used to analyze via the GP an experimental situation on the interface between quantum mechanics and general relativity. Moreover, by scanning θ around $\pi/2$ (i.e., change the relative populations of the $|1\rangle$ and $|2\rangle$ states from below to above half), one should observe a sign change that may allow the construction of a novel type of gravitational sensor. A main limitation that will have to be examined is the sharpness of the slope. Even when working at the best point ($\Delta\Phi = \pi$; see Fig. 4B), the practical slope will never be the theoretical infinite slope, as the visibility at this exact point is zero (as may be seen from the large error bar). However, the visibility quickly recovers and numerical and experimental studies are needed to reveal the ultimate realizable slope. An additional limitation has to do with the fact that the sharp slope appears when $\Delta\phi = \pi$, so when dealing with proper time differences that give rise to a substantially different $\Delta\phi$, a bias would have to be introduced to keep the system at this optimal point, and this bias may introduce its own errors.

METHODS

Detailed experimental scheme

The experiment was realized in an atom chip setup (39). We present the detailed experimental scheme in fig. S1, which includes the two-level system preparation. We first prepared a Bose-Einstein condensate (BEC) of about 10^{4-87} Rb atoms in the state $|2\rangle \equiv |F=2, m_F=2\rangle$ in a magnetic trap located $90\ \mu\text{m}$ below the chip surface. After the BEC atoms were released from the trap, the entire experimental sequence took place in the presence of a homogeneous magnetic bias field of $36.7\ \text{G}$ in the y direction (z is the direction of gravity), which created an effective two-level system (with $|1\rangle \equiv |F=2, m_F=1\rangle$) via the nonlinear Zeeman effect with $E_{ij} = E_{21} \approx h \times 25\ \text{MHz}$ (where i and j are the m_F numbers, all in the $F=2$ manifold), and $E_{21} - E_{10} \approx h \times 180\ \text{kHz}$. We then applied an RF pulse (duration TR_1 , where typically $10\ \mu\text{s}$ gives rise to a $\theta = \pi/2$ rotation) to prepare a spin superposition ($|1\rangle + |2\rangle)/\sqrt{2}$ between the $|2\rangle$ and $|1\rangle$ states. A magnetic gradient pulse $\partial B/\partial z$ of duration $TG_1 = 4\ \mu\text{s}$, generated by currents in the atom chip wires, was applied to create the Stern-Gerlach splitting, in which the different spins are exposed to differential forces. To enable interference between the two wave packets ($|2\rangle$ and $|1\rangle$ are orthogonal), a second $\pi/2$ pulse (TR_2) was applied to mix the spins. To stop the relative velocity of the wave packets, a second magnetic gradient pulse (TG_2) was applied to yield differential forces for the same-spin states at different locations. A spatial superposition of two wave packets in state $|2\rangle$ now exists (separated along the z axis, with zero relative velocity). Note that during TG_2 , the $|1\rangle$ state from the two wave packets was pushed outside the experimental zone. The control of θ introduced in Fig. 1A is realized by a third RF pulse of duration TR_3 (T_R in the main text). The relative rotation between the two wave packets $\Delta\phi$ may be changed by applying a third magnetic field gradient of duration TG_3 (T_G in the main text). The wave packets were then allowed to expand (during time of flight of $\sim 10\ \text{ms}$, much larger than the re-

ciprocal of the trap frequency $\sim 500\ \text{Hz}$) and overlap to form the interference pattern. An image based on the absorption imaging was taken in the end.

The magnetic gradient pulses were generated by three parallel gold wires located on the chip surface with a length of $10\ \text{mm}$, a width of $40\ \mu\text{m}$, and a thickness of $2\ \mu\text{m}$. The chip wire current was driven using a simple 12.5-V battery and modulated using a home-made current shutter. The three parallel gold wires were separated by $100\ \mu\text{m}$ (center to center), and the same current runs through them in alternating directions. The benefit of using this three-wire configuration instead of a single gold wire is that a two-dimensional quadrupole field was created at $z = 100\ \mu\text{m}$ below the atom chip. As the magnetic instability is proportional to the field strength, and as the main instability originates in the gradient pulses (the bias fields from external coils are very stable), positioning the atoms near the middle (zero) of the quadrupole field significantly reduces the magnetic noise while maintaining the strength of the magnetic gradients.

Determination of the population transfer and the value of θ

In Fig. 5, we explained how the values of θ are obtained from the measurement of population transfer when we apply TR_3 (T_R in the main text). Stern-Gerlach splitting was used to separate the $m_F = 1$ and $m_F = 2$ parts, and absorption imaging was performed to evaluate the atom number. See the details in the figure caption.

The CCD image of the interference pattern while θ is scanned

In Fig. 6, we showed the raw data of the interference patterns, which are displayed in Fig. 2 (averaged over numerous values of θ) and in Fig. 3B (where the phase for different values of θ is presented), when TG_3 (T_G in the main text) equals $17\ \mu\text{s}$ ($\Delta\phi \approx \pi$). The whole scanning range of T_R is $40\ \mu\text{s}$, corresponding to one full cycle (2π) of the Rabi oscillation. The phase of the interference pattern was found to be rigid when the Bloch vector is located in the northern hemisphere or in the southern hemisphere, with a π phase jump in between.

The interference pattern was fitted with the function $A \exp\left[-\frac{(z - z_{\text{CM}})^2}{2\sigma_z^2}\right] \left\{1 + v \sin\left[\frac{2\pi}{\lambda}(z - z_{\text{ref}}) + \Phi\right]\right\} + c$, where A is a constant related the optical density in the system, z_{CM} is the center-of-mass (CM) position of the combined wave packet at the time of imaging, σ_z is the Gaussian width of the combined wave packet obtained after time of flight, $\lambda = \frac{ht}{md}$ is the fringe periodicity, v is the visibility, z_{ref} is a fixed reference point, c is the background optical density from the absorption imaging, and Φ is the phase of the interference pattern that appears in Eq. 2. In the fringe periodicity $\lambda = \frac{ht}{md}$, h is the Planck constant, t is the duration of time of flight, m is the mass of ^{87}Rb atom, and d is the distance between the two wave packets. In Fig. 3, we measure the dependence of Φ on θ (T_R) for a fixed T_G and then fit the data to Eq. 2, returning values for both ϕ_0 and $\Delta\phi$.

Geometrical phases for different values of $\Delta\phi$

Here, we describe the approach used to derive the expression of Φ_G in Eq. 3. Mukunda and Simon (37) developed a general formalism called the quantum kinematic approach for the GP in quantum systems.

In the formalism of Mukunda and Simon, a one-parameter smooth curve was defined from a vector ψ belonging to a Hilbert space \mathcal{H} , $\mathcal{C} = \{\psi(s) \in \mathcal{N}_0, s \in [s_1, s_2]\}$. \mathcal{N}_0 is the subset of unit vectors of \mathcal{H} . Note that the curve \mathcal{C} is not necessarily closed. The only requirements of the theory are the smoothness of \mathcal{C} , i.e., $\psi(s)$ should be

differentiable, and the non-orthogonality of the initial and final states. The GP is given by

$$\Phi_G = \Phi - \Phi_D \quad (4)$$

where Φ is the total phase. Φ_D is the dynamical phase arising from the energy dependence on s during the evolution. This general formalism naturally reduces to the evolution under the time-dependent Schrödinger equation if the parameter s is time. The curve \mathcal{C} is the trajectory of the wave function during the propagation time $0 \leq t \leq T$.

The total phase Φ during an evolution along \mathcal{C} is given by

$$\Phi = \arg \langle \psi(s_1) | \psi(s_2) \rangle \quad (5)$$

Taking $\psi(s) = \left(\cos \frac{\theta}{2} | 2 \rangle + \exp(is\Delta\phi) \sin \frac{\theta}{2} | 1 \rangle \right)$ and $\{s_1, s_2\} = [0, 1]$, we found for the total phase

$$\Phi = \arctan \left\{ \frac{\sin^2(\theta/2) \sin \Delta\phi}{\cos^2(\theta/2) + \sin^2(\theta/2) \cos \Delta\phi} \right\} \quad (6)$$

where we should add to Φ the phase ϕ_0 arising from the evolution of the spatial part. This yields Eq. 2.

The dynamical phase Φ_D can be calculated from the integral of the evolution curve \mathcal{C} (7)

$$\Phi_D = \text{Im} \int_{s_1}^{s_2} \langle \psi(s) | \dot{\psi}(s) \rangle ds \quad (7)$$

We find

$$\Phi_D = \frac{\Delta\phi}{2} (1 - \cos \theta) \quad (8)$$

to which phase ϕ_0 should also be added. Subtracting Φ_D from Φ yields the expression for Φ_G of Eq. 3. Φ_G is more suitable to use for analysis because gauge-dependent phases in Φ and Φ_D mutually cancel.

In fig. S2, we presented the detailed theoretical behavior of Φ_G (Eq. 3) as a function of θ and $\Delta\phi$. The characteristics of Φ_G are the singularity at $\Delta\phi = \pi$ and $\theta = (n + 1/2)\pi$ (where n is an integer), and the change of sign when θ goes across these values. This result was originally obtained from (10) (see figure 4 in this reference).

SUPPLEMENTARY MATERIALS

Supplementary material for this article is available at <http://advances.sciencemag.org/cgi/content/full/6/9/eaay8345/DC1>

Fig. S1. Detailed scheme of the spatial SU(2) interferometer.

Fig. S2. Theoretical curves of the GP Φ_G versus θ for different values of $\Delta\phi$.

REFERENCES AND NOTES

- S. Pancharatnam, Generalized theory of interference, and its applications. *Proc. Indian Acad. Sci.* **44**, 247–262 (1956).
- M. V. Berry, Quantal phase factors accompanying adiabatic changes. *Proc. R. Soc. London A* **392**, 45–57 (1984).
- G. Herzberg, H. C. Longuet-Higgins, Intersection of potential energy surfaces in polyatomic molecules. *Discuss. Faraday Soc.* **35**, 77–82 (1963).
- B. Simon, Holonomy, the quantum adiabatic theorem, and Berry's phase. *Phys. Rev. Lett.* **51**, 2167 (1983).
- F. Wilczek, A. Zee, Appearance of gauge structure in simple dynamical systems. *Phys. Rev. Lett.* **52**, 2111 (1984).
- Y. Aharonov, J. Anandan, Phase change during a cyclic quantum evolution. *Phys. Rev. Lett.* **58**, 1593 (1987).
- J. Samuel, R. Bhandari, General setting for Berry's phase. *Phys. Rev. Lett.* **60**, 2339 (1988).
- M. V. Berry, Anticipations of the geometric phase. *Phys. Today* **43**, 34 (1990).
- M. V. Berry, The adiabatic phase and Pancharatnam's phase for polarized light. *J. Mod. Opt.* **34**, 1401–1407 (1987).
- R. Bhandari, SU(2) phase jumps and geometric phases. *Phys. Lett. A* **157**, 221–225 (1991).
- T. Bitter, D. Dubbers, Manifestation of Berry's topological phase in neutron spin rotation. *Phys. Rev. Lett.* **59**, 251 (1987).
- R. Bhandari, J. Samuel, Observation of topological phase by use of a laser interferometer. *Phys. Rev. Lett.* **60**, 1211 (1988).
- P. J. Leek, J. M. Fink, A. Blais, R. Bianchetti, M. Göppel, J. M. Gambetta, D. I. Schuster, L. Frunzio, R. J. Schoelkopf, A. Wallraff, Observation of Berry's phase in a solid-state qubit. *Science* **318**, 1889–1892 (2007).
- M. D. Schroer, M. H. Kolodrubetz, W. F. Kindel, M. Sandberg, J. Gao, M. R. Vissers, D. P. Pappas, A. Polkovnikov, K. W. Lehnert, Measuring a topological transition in an artificial spin-1/2 system. *Phys. Rev. Lett.* **113**, 050402 (2014).
- P. Roushan, C. Neill, Y. Chen, M. Kolodrubetz, C. Quintana, N. Leung, M. Fang, R. Barends, B. Campbell, Z. Chen, B. Chiaro, A. Dunswoth, E. Jeffrey, J. Kelly, A. Megrant, J. Mutus, P. J. J. O'Malley, D. Sank, A. Vainsencher, J. Wenner, T. White, A. Polkovnikov, A. N. Cleland, J. M. Martinis, Observation of topological transitions in interacting quantum circuits. *Nature* **515**, 241–244 (2014).
- C. Zu, W.-B. Wang, L. He, W.-G. Zhang, C.-Y. Dai, F. Wang, L.-M. Duan, Experimental realization of universal geometric quantum gates with solid-state spins. *Nature* **514**, 72–75 (2014).
- E. Sjöqvist, D. M. Tong, L. M. Andersson, B. Hessmo, M. Johansson, K. Singh, Non-adiabatic holonomic quantum computation. *New J. Phys.* **14**, 103035 (2012).
- E. Sjöqvist, Geometric phases in quantum information. *Int. J. Quantum Chem.* **115**, 1311–1326 (2015).
- S. J. Glaser, U. Boscain, T. Calarco, C. P. Koch, W. Köckenberger, R. Kosloff, I. Kuprov, B. Luy, S. Schirmer, T. Schulte-Herbrüggen, D. Sugny, F. K. Wilhelm, Training Schrödinger's cat: Quantum optimal control. *Eur. Phys. J. D* **69**, 279 (2015).
- K. Xu, T. Xie, F. Shi, Z.-Y. Wang, X. Xu, P. Wang, Y. Wang, M. B. Plenio, J. Du, Breaking the quantum adiabatic speed limit by jumping along geodesics. *Sci. Adv.* **5**, eaax3800 (2019).
- C. W. Chou, D. B. Hume, T. Rosenband, D. J. Wineland, Optical clocks and relativity. *Science* **329**, 1630–1633 (2010).
- T. van Dijk, H. F. Schouten, T. D. Visser, Geometric interpretation of the Pancharatnam connection and non-cyclic polarization changes. *J. Opt. Soc. Am. A* **27**, 1972–1976 (2010).
- A. Morinaga, A. Monma, K. Honda, M. Kitano, Berry's phase for a noncyclic rotation of light in a helically wound optical fiber. *Phys. Rev. A* **76**, 052109 (2007).
- T. van Dijk, H. F. Schouten, W. Ubachs, T. D. Visser, The Pancharatnam-Berry phase for non-cyclic polarization changes. *Opt. Express* **18**, 10796–10804 (2010).
- A. G. Wagh, V. C. Rakhecha, P. Fischer, A. Ioffe, Neutron interferometric observation of non-cyclic phase. *Phys. Rev. Lett.* **81**, 1992 (1998).
- S. Filipp, Y. Hasegawa, R. Loidl, H. Rauch, Non-cyclic geometric phase due to spatial evolution in a neutron interferometer. *Phys. Rev. A* **72**, 021602(R) (2005).
- A. Morinaga, K. Nanri, Noncyclic Berry phase and scalar Aharonov-Bohm phase for the spin-redirected evolution in an atom interferometer. *Phys. Rev. A* **86**, 022105 (2012).
- A. Morinaga, K. Nanri, Erratum: Noncyclic Berry phase and scalar Aharonov-Bohm phase for the spin-redirected evolution in an atom interferometer. *Phys. Rev. A* **94**, 019907 (2016).
- R. Bhandari, Comment on "neutron interferometric observation of non-cyclic phase". *Phys. Rev. Lett.* **83**, 2089 (1999).
- A. G. Wagh, V. Chand Rakhecha, P. Fischer, A. Ioffe, Wagh et al. reply. *Phys. Rev. Lett.* **83**, 2090 (1999).
- A. Takahashi, H. Imai, K. Numazaki, A. Morinaga, Phase shift of an adiabatic rotating magnetic field in Ramsey atom interferometry for $m = 0$ sodium-atom spin states. *Phys. Rev. A* **80**, 050102(R) (2009).
- A. D. Cronin, J. Schmiedmayer, D. E. Pritchard, Optics and interferometry with atoms and molecules. *Rev. Mod. Phys.* **81**, 1051 (2009).
- G. M. Tino, M. A. Kasevich, Atom Interferometry, in *Proceedings of the International School of Physics "Enrico Fermi"* (IOS Press, 2014), vol. 188.
- S. Machluf, Y. Japha, R. Folman, Coherent Stern-Gerlach momentum splitting on an atom chip. *Nat. Commun.* **4**, 2424 (2013).
- Y. Margalit, Z. Zhou, S. Machluf, D. Rohrlich, Y. Japha, R. Folman, A self-interfering clock as a "which path" witness. *Science* **349**, 1205–1208 (2015).
- Z. Zhou, Y. Margalit, D. Rohrlich, Y. Japha, R. Folman, Quantum complementarity of clocks in the context of general relativity. *Class. Quantum Grav.* **35**, 185003 (2018).
- N. Mukunda, R. Simon, Quantum kinematic approach to the geometric phase. I. General formalism. *Ann. Phys. Rehabil. Med.* **228**, 205–268 (1993).
- F. De Zela, The Pancharatnam-Berry phase: Theoretical and experimental aspects, in *Theoretical Concepts of Quantum Mechanics*, M. R. Pahlavani, Ed. (InTech, 2012).
- M. Keil, O. Amit, S. Zhou, D. Groswasser, Y. Japha, R. Folman, Fifteen years of cold matter on the atom chip: Promise, realizations, and prospects. *J. Mod. Opt.* **63**, 1840–1885 (2016).

Acknowledgments: We thank the BGU nano-fabrication facility for the high-quality chip.

Funding: This work was funded, in part, by the Israel Science Foundation (grants no. 292/15 and 856/18), the German-Israeli DIP project (Hybrid devices: FO 703/2-1) supported by the DFG, and the European ROCIT consortium for stable optical clocks. We also acknowledge support from the Israeli Council for Higher Education and from the Ministry of Immigrant Absorption (Israel). **Author contributions:** Z.Z. and Y.Ma. did the experiment. Z.Z., S.M., and Y.Me. did the theory. All authors discussed the results and participated in the writing of the manuscript. R.F. supervised the experiment, the theory, and the writing of the manuscript.

Competing interests: The authors declare that they have no competing interests. **Data and Materials availability:** All data needed to evaluate the conclusions in the paper are present in

the paper and/or the Supplementary Materials. Additional data related to this paper may be requested from the authors.

Submitted 22 July 2019

Accepted 4 December 2019

Published 28 February 2020

10.1126/sciadv.aay8345

Citation: Z. Zhou, Y. Margalit, S. Moukouri, Y. Meir, R. Folman, An experimental test of the geodesic rule proposition for the noncyclic geometric phase. *Sci. Adv.* **6**, eaay8345 (2020).

An experimental test of the geodesic rule proposition for the noncyclic geometric phase

Zhifan ZhouYair MargalitSamuel MoukouriYigal MeirRon Folman

Sci. Adv., 6 (9), eaay8345. • DOI: 10.1126/sciadv.aay8345

View the article online

<https://www.science.org/doi/10.1126/sciadv.aay8345>

Permissions

<https://www.science.org/help/reprints-and-permissions>

Use of this article is subject to the [Terms of service](#)

Science Advances (ISSN 2375-2548) is published by the American Association for the Advancement of Science. 1200 New York Avenue NW, Washington, DC 20005. The title *Science Advances* is a registered trademark of AAAS.

Copyright © 2020 The Authors, some rights reserved; exclusive licensee American Association for the Advancement of Science. No claim to original U.S. Government Works. Distributed under a Creative Commons Attribution License 4.0 (CC BY).